Hourglasslike nodal net semimetal in Ag$_2$BiO$_3$

Botao Fu, Xiaotong Fan, Dashuai Ma, Cheng-Cheng Liu,[*] and Yugui Yao[†]

Beijing Key Laboratory of Nanophotonics and Ultrafine Optoelectronic Systems, School of Physics,
Beijing Institute of Technology, Beijing 100081, China

Based on first-principles calculations and analysis of crystal symmetries, we propose a kind of hourglasslike nodal net (HNN) semimetal in centrosymmetric Ag$_2$BiO$_3$ that is constructed by two hourglasslike nodal chains at mutually orthogonal planes in the extended Brillouin zone (BZ) when the weak spin-orbit coupling (SOC) mainly from the 6s orbital of Bi atoms is ignored. The joint point in the nodal net structure is a special double Dirac point located at the BZ corner. Different from previous HNNs [T. Bzdušek *et al.*, Nature (London) **538**, 75 (2016)] where the SOC and double group nonsymmorphic symmetries are necessary and also different from the accidental nodal net, this HNN structure is inevitably formed and guaranteed by spinless nonsymmorphic symmetries and thus robust against any symmetry-remaining perturbations. The Fermi surface in Ag$_2$BiO$_3$ consisting of a toruslike electron pocket and a toruslike hole pocket may lead to unusual transport properties. A simple four-band tight-binding model is built to reproduce the HNN structure. For a semi-infinite Ag$_2$BiO$_3$, the "drumhead"-like surface states with nearly flat dispersions are demonstrated on (001) and (100) surfaces, respectively. If such a weak-SOC effect is taken into consideration, this HNN structure will be slightly broken, leaving a pair of hourglasslike Dirac points at the twofold screw axis. This type of hourglasslike Dirac semimetal is symmetry enforced and does not need band inversion anymore. Our discovery provides a platform to study novel topological semimetal states from nonsymmorphic symmetries.

I. INTRODUCTION

Beyond the famous Dirac and Weyl semimetals [1–5] which can be regarded as analogs of Dirac and Weyl fermions in particle physics, a new kind of topological semimetal, a nodal line semimetal (NLSM) [6–13], was recently predicted and experimentally discovered [14–17]. For a NLSM, the lowest conduction and highest valence bands touch each other at a series of continuous points, forming a closed loop in reciprocal space. The topological property of the NLSM can be characterized by the accumulation of Berry phase [18] along a closed loop encircling the nodal line. According to bulk-boundary correspondence, a NLSM can exhibit a "drumhead"-like surface state with nearly flat dispersion which may induce giant Friedel oscillations [19], strong correlated effects, and high-temperature superconductivities [20]. With a toruslike Fermi surface, a NLSM shows unusual transport properties such as multiple phase shifts in quantum oscillations [21,22].

According to the robustness, NLSMs can be divided into two categories: accidental nodal lines (ANLs) and symmetry-enforced nodal lines. The ANLs are usually derived from the band-inversion mechanism and protected by the coexistence of time-reversal and space-inversion symmetries [23–26] or mirror symmetry [27,28]. This type of nodal line can be annihilated without breaking the corresponding symmetry as long as the band inversion disappears. On the other hand, a

nonsymmorphic symmetry can protect the symmetry-enforced nodal line. Suppose there is a slide mirror operation $g_1 = \{M_z | \boldsymbol{a}/2\}$, indicating a mirror reflection about the z direction accompanied by a translation of half the lattice vector $\boldsymbol{a}/2$. On the mirror-invariant plane (e.g., $k_z = 0$), the momentum-dependent eigenvalues of g_1 are $\pm \lambda e^{ik_x/2}$, where $\lambda = 1$ or i for spinless or spinful systems. As shown in Fig. 1(a), for systems with time-reversal symmetry (TRS) T but without space-inversion symmetry P, all bands generally split except at time-reversal-invariant momenta (TRIMs), where $T^2 = -1$ ensures the Kramers degeneration. Based on the evolution of the eigenvalues between two TRIMs (e.g., the Γ and X points), two pairs of bands have to switch their partners and inevitably cross each other, forming hourglasslike band structures [29]. Actually, along any loops connecting these two TRIMs in the plane, the band degenerate point always exists, which will form a closed nodal ring (red solid line) centered at the Γ point, as displayed in the right panel of Fig. 1(a). Moreover, if the system has an additional glide operation on the perpendicular plane (e.g., the k_x-k_z plane), another nodal ring (green dashed line) will appear, and the two nodal rings touch each other to form an hourglasslike nodal chain (HNC) structure [30,31], as shown in the right panel of Fig. 1(a). This symmetry-enforced nodal line and nodal chain were first put forward in Ref. [30], and IrF$_4$ was proposed as a candidate material. However, the symmetry-enforced nodal lines in the material are subject to three constraints: a remarkable spin-orbit coupling (SOC) effect, broken inversion symmetry, and preserved time-reversal symmetry. The third constraint may be broken by the possible magnetic order in IrF$_4$ at low temperature. As a result, it is important and urgent
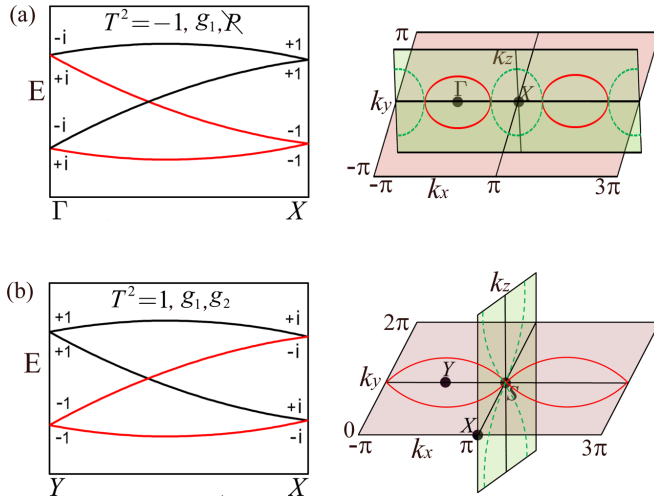
FIG. 1. (a) Left: the hourglasslike band structures protected by $g_1 = \{M_z|\boldsymbol{a}/2\}$ for systems without P symmetry including the SOC effect. Right: the corresponding nodal rings at the k_x-k_y plane (red solid line) and the k_x-k_z plane (green dashed line) constructing an HNC in the extended BZ. (b) Left: hourglasslike band structures without SOC protected by g_1 and g_2 in the absence of SOC effect. Right: the corresponding HNCs at the k_x-k_y plane (red solid line) and the k_x-k_z (green dashed line) constructing an HNN structure in the extended BZ. The eigenvalues of $\{M_z|\boldsymbol{a}/2\}$ are given. Notice that the HNC in (b) is formed by a large nodal line traversing the whole BZ, while the HNC in (a) is formed by two tangent nodal rings alternately in orthogonal planes.

to search for more and better symmetry-enforced nodal line semimetal candidates free of such constraints.

In this work, we find another path to realize symmetry-enforced nodal lines and nets in weak SOC materials with spinless nonsymmorphic symmetries, which can be generalized to bosonic systems with similar symmetries. As shown in the left panel of Fig. 1(b), in the absence of SOC, $T^2 = 1$ does not ensure Kramers degeneracy anymore. However, the joint operation $\widetilde{T} = g_1 T$ satisfies $\widetilde{T}^2 = -1$ at $k_x = \pi$, which can give equivalent Kramers degeneracy at the X point. If we have another nonsymmorphic symmetry g_2 (e.g., a twofold screw axis) that can ensure the double degeneracy at $k_x = 0$ (e.g., the Y point), then following the evolution of the eigenvalues of g_1 from Y to X, we deduce that a nodal line will appear in the $k_z = 0$ plane. In fact, as shown in the right panel of Fig. 1(b), rather than forming a nodal line, here the crossing point begins and ends at a fourfold-degenerate point on the Brillouin zone (BZ) corner (this will be discussed later) and finally forms an HNC structure (red solid line) in the extended BZ. If we further consider an extra perpendicular slide mirror plane, another HNC (green dashed line) emerges, and two HNCs will link together, forming a nodal net structure. From this analysis, we propose that Ag_2BiO_3 with the $Pnna$ space group can host an ideal hourglasslike nodal net (HNN) structure when the weak SOC effect is ignored. The Fermi surface is made up of a toruslike electron pocket and a toruslike hole pocket, which may induce novel transport properties. After including the SOC effect, the HNN is slightly gapped, and a pair of hourglasslike Dirac points consequentially emerge, which are

distinct from previous Dirac semimetals protected by pure rotation symmetries [32].

II. THE CALCULATION METHOD AND THE GEOMETRIC STRUCTURE OF Ag_2BiO_3

Our first-principles calculations were performed using the Vienna Ab initio Simulation Package (VASP) [33,34] within the generalized gradient approximation [35] of Perdew, Burke, and Ernzerhof [36]. A cutoff energy of 500 eV and a k mesh of $15 \times 15 \times 15$ are chosen to guarantee energy convergence. The crystal structure is relaxed to the ground states with a force of less than 0.01 eV/Å on each atom. The surface states are obtained using the method of maximally localized Wannier functions in the WANNIER90 [37,38] code and WannierTools code [39].

The crystal structure of Ag_2BiO_3 [40] used to be very controversial because of the discrepancy between theoretically predicted metallic behaviors and experimentally observed insulating results. Subsequently, some careful analyses both experimentally and theoretically verified that Ag_2BiO_3 has three distinctive phases [41,42] with space groups of $Pnna$, $Pnn2$, and Pn. The $Pnna$ phase is a metal, and the Pn phase is a semiconductor, both of which are metastable and can transform into the $Pnn2$ phase, which is a semiconducting ground state. Very recently, an electric-field-induced metal-insulator transition and Weyl semimetal were proposed in the $Pnn2$ phase of Ag_2BiO_3 [43]. In this work, we just focus on the $Pnna$ phase, and the formula Ag_2BiO_3 refers to the $Pnna$ phase unless specifically stated otherwise.

As shown in Fig. 2(a), Ag_2BiO_3 crystallizes in a tetragonal crystal with the centrosymmetric nonsymmorphic space group $Pnna$ (No. 52). There are four bismuth atoms (violet balls) in the unit cell that are located at the octahedral center of the oxygen atoms (red balls), and eight silver atoms (gray balls) fill the interstice sites. The optimized lattice constants are $|\boldsymbol{a}| = 6.13$ Å, $|\boldsymbol{b}| = 6.36$ Å, and $|\boldsymbol{c}| = 9.83$ Å, which are consistent with the experimental result [40]. The Brillouin zone and high-symmetry points are displayed in Fig. 2(b).

III. THE ELECTRONIC STRUCTURE OF Ag_2BiO_3

The calculated electronic structure of Ag_2BiO_3 in the absence of SOC is shown in Fig. 2(c). We can see there are four bands entangled together near the Fermi level which are mainly derived from the $6s$ orbital of bismuth atoms. In addition, due to nonsymmorphic symmetries in the $Pnna$ space group, both the conduction and valence bands possess twofold degeneracy at the high-symmetry points (X, Y, R, S, etc.), lines (XS, SY, RS, etc.), and plane ($RTYS$) in the BZ, as shown in Figs. 2(c) and 2(e). On the one hand, along the X-S-Y path, the lowest twofold-degenerate conduction and highest valence bands touch at the S point at the Fermi level and form a fourfold-degenerate Dirac point. In analogy with the concept of a double Dirac point [44,45] in the presence of SOC, we denote this fourfold-degenerate Dirac point in the absence of SOC as double Dirac point. On the other hand, along the $Y\Gamma$ and UR paths, two singlet bands cross each other, forming a single Dirac point located slightly below and above the Fermi level.
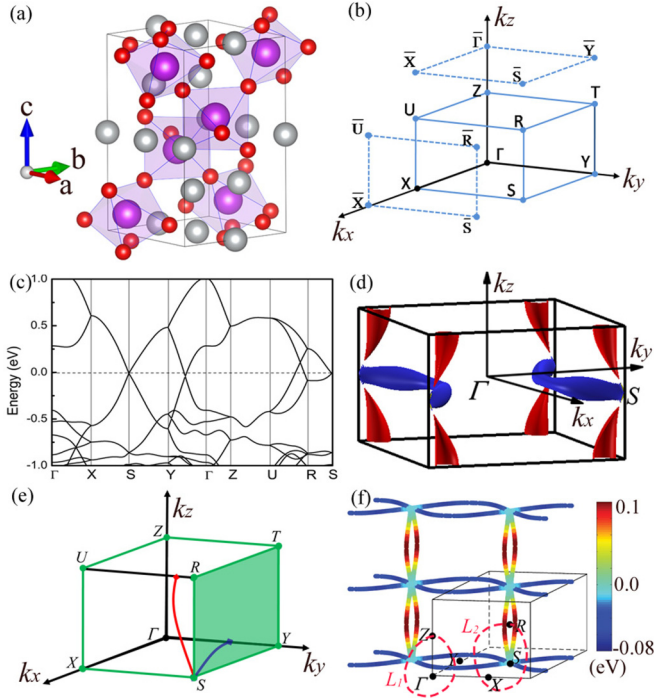
FIG. 2. (a) The unit cell of Ag_2BiO_3 in the $Pnna$ phase. The violet, red, and gray balls represent bismuth, oxygen, and silver atoms, respectively. (b) The bulk Brillouin zone and (001)/(100) surface Brillouin zone. (c) The band structure of Ag_2BiO_3 without SOC. (d) The toruslike Fermi surface with electron (red) and hole (blue) pockets. (e) All the twofold-degenerate points (green) and two nodal lines (red and blue) in the BZ. (f) Display of the HNN structure in the extended BZ. The color stands for the energy dispersion of the HNN with respect to the Fermi level. The red dashed lines labeled L_1, L_2 represent two distinctive loops along which the Berry phase is calculated.

Remarkably, the band connection of the four bands near the Fermi level shows the typical hourglasslike shape.

Moreover, through careful calculation, we discover that the trace of the Dirac points actually forms a nodal line (NL) located in the $X\Gamma YS$ ($k_z = 0$) and $XURS$ ($k_x = \pi$) planes. Displayed in Fig. 2(e), the NL at the $XURS$ plane starts from the S point, passes through UR, and comes back to the next S point in the extended BZ, which actually forms an HNC structure along the SR direction, as depicted in the right panel of Fig. 1(b). On the other hand, the NL in the $X\Gamma YS$ plane also starts at the S point, crosses ΓY, and forms another HNC structure along the SY direction. Those two HNCs joint together at the double Dirac point S and thus form a unique HNN structure, as plotted in Fig. 2(f). Based on the Berry phase calculation along distinctive loops [red dashed lines L_1 and L_2 in Fig. 2(f)], we obtain π and zero Berry phase for the L_1 and L_2 paths, respectively. The L_1 path encircles the nodal line one time, while L_2 encircles the nodal line two times. It is significant to find that the HNCs constructing the HNN structure have different energies. One HNC on the $k_z = 0$ plane has almost negative energy, while the other on the $k_x = \pi$ plane has nearly positive energy with respect to the Fermi level. By plotting the Fermi surface in Fig. 2(d), we find a toruslike electron pocket (in blue) originating from the HNC

at the $k_z = 0$ plane and a hole pocket (in red) originating from the HNC at the $k_x = \pi$ plane. From this perspective, two HNCs constructing an HNN are separated both in momentum space and in energy space except around the S point. As far as we know, the HNN structure proposed in this paper is different from all known nodal line, nodal chain, and nodal net [46–48] systems, and we hope this unique HNN structure will result in novel properties in future transport experiments.

IV. SYMMETRY ANALYSIS OF Ag_2BiO_3

As mentioned before, the emergence of an HNN semimetal in Ag_2BiO_3 without SOC results from specific nonsymmorphic symmetries. Based on symmetry analysis, we are going to prove the existence of an HNN structure in Ag_2BiO_3 with the space group $Pnna$. The $Pnna$ space group includes eight symmetry operations in total: I, P, $\{C_{2x}|\boldsymbol{b}/2 + \boldsymbol{c}/2\}$, $\{C_{2z}|\boldsymbol{a}/2\}$, $\{C_{2y}|\boldsymbol{a}/2 + \boldsymbol{b}/2 + \boldsymbol{c}/2\}$, $\{M_x|\boldsymbol{b}/2 + \boldsymbol{c}/2\}$, $\{M_y|\boldsymbol{a}/2 + \boldsymbol{b}/2 + \boldsymbol{c}/2\}$, and $\{M_z|\boldsymbol{a}/2\}$, where the first is the identity operation, the second is the inversion operation, and the third and the fourth are twofold rotations along the x and z axes, respectively. The last four are effective nonsymmorphic operations.

First, to prove the double degeneracy of the band structure at BZ boundaries, we consider a nonsymmorphic operation $g_1 = \{M_z|\boldsymbol{a}/2\}$ and TRS T, which jointly act on the lattice momentum as follows:

$$g_1 : (k_x, k_y, k_z) \rightarrow (k_x, k_y, -k_z), \tag{1}$$

$$T : (k_x, k_y, -k_z) \rightarrow (-k_x, -k_y, k_z). \tag{2}$$

Defining a joint operation $\widetilde{T} = g_1 T$, we find it commutes with the Hamiltonian $H(\boldsymbol{k})$ when $\boldsymbol{k} = (0/\pi, 0/\pi, k_z)$. On the other band, with the conditions $T^2 \equiv 1$ and $g_1^2 = e^{ik_x}$, we can get $\widetilde{T}^2 = -1$ when $k_x = \pi$. As a result, the Kramers-like band degeneracy [29] can be obtained along the XU ($\pi, 0, k_z$) and RS (π, π, k_z) paths. Similarly, the operation $g_2 = \{M_y|\boldsymbol{a}/2 + \boldsymbol{b}/2 + \boldsymbol{c}/2\}$ guarantees band degeneracy along the ZT and XS paths, and the operation $g_3 = \{M_x|\boldsymbol{b}/2 + \boldsymbol{c}/2\}$ enforces band degeneracy along the ZU and YS paths. In addition, the twofold screw axis $g_4 = \{C_{2y}|\boldsymbol{a}/2 + \boldsymbol{b}/2 + \boldsymbol{c}/2\}$ enforces band degeneracy in the whole $RTYS$ ($k_y = \pi$) plane. Those degenerating points in the BZ are clearly demonstrated in Fig. 2(e).

Second, to prove the fourfold degeneracy at the S ($\pi, \pi, 0$) point, we chose three symmetry operations: P, g_2, and $g_5 = \{C_{2z}|\boldsymbol{a}/2\}$, which all commute with $H(\boldsymbol{k})$ at the S point. It is easy to obtain the relations $P^2 = 1$, $g_2^2 = -1$, and $g_5^2 = 1$. In analogy with the above analysis, combining $g_2^2 = -1$ with T, we can acquire two Kramers-like degenerate states, such as $|\phi_{+i}^E\rangle$ and $T|\phi_{+i}^E\rangle$ with eigenvalues $+i$ and $-i$ of g_2, respectively. Utilizing the commutation relation $[P, g_2] = 0$, we can additionally label those states by the parity λ as $|\phi_{\lambda,+i}^E\rangle$, $T|\phi_{\lambda,+i}^E\rangle$. Since T will not change parity, those two states must have the same parity. On the other band, using the anticommutation relation $\{P, g_5\} = 0$, we can deduce that $|\phi_{\lambda,+i}^E\rangle$ ($T|\phi_{\lambda,+i}^E\rangle$) must have the degenerate partner $g_5|\phi_{\lambda,+i}^E\rangle$ ($g_5 T|\phi_{\lambda,+i}^E\rangle$) with opposite parity. Therefore, we obtain the fourfold degeneracy of Bloch states at the S point.
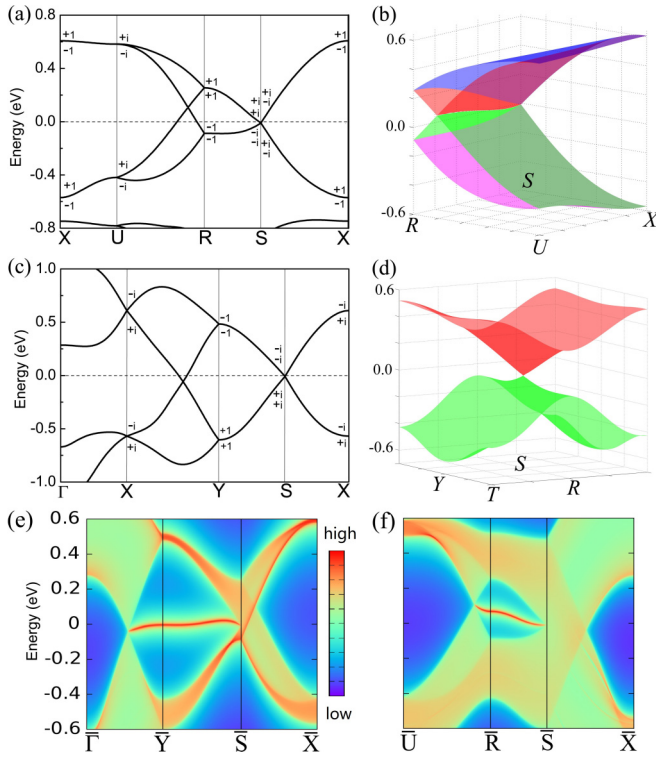
FIG. 3. (a) The band structure at the $XURS$ plane. The eigenvalues of $\{M_x|\boldsymbol{b}/2 + \boldsymbol{c}/2\}$ are shown. (b) Three-dimensional view of the energy spectrum at the $XURS$ plane. (c) The band structure at the $X\Gamma YS$ plane. The eigenvalues of $\{M_z|\boldsymbol{a}/2\}$ are shown. (d) Three-dimensional view of the double Dirac cone around the S point at the $RTYS$ plane. The bands are doubly degenerate. (e) and (f) Calculated surface states of Ag_2BiO_3 on the (001) and (100) surfaces, respectively. The color represents the weight of the local density of states.

Keeping the above two conclusions in mind, we now discuss the band connections and corresponding band crossings in each mirror-invariant plane. For the $g_3 = \{M_x|\boldsymbol{b}/2 + \boldsymbol{c}/2\}$ operation, the invariant plane is $XURS$ ($k_x = \pi$), and we can use its eigenvalues $g_\pm(k_y, k_z) = \pm e^{ik_y/2 + ik_z/2}$ to identify each band. Specifically, at U $(\pi, 0, \pi)$ and S $(\pi, \pi, 0)$, a pair of degenerate bands have opposite eigenvalues $(\pm i)$, which are interchanged by T. However, at the X $(\pi, 0, 0)$ and R (π, π, π) points, the eigenvalues can take $+1$ or -1. Because the bands are doubly degenerate along the UX path, the eigenvalues for a pair of degenerate bands will evolve from $\pm i$ at the U point to ± 1 at the X point. Therefore, the quadruply degenerate states at the S point with eigenvalues $(+i, -i, +i, -i)$ will split into two pairs of doubly degenerate states along the SX path with eigenvalues $(+i, -i)$ and $(+i, -i)$, respectively, as shown in Fig. 3(a). On the other hand, since the degeneracy along the SR path is protected by g_4T, which commutes with g_3 at the R point, we can easily find that the doubly degenerate bands at the R point have the same eigenvalues, $(+1, +1)$ or $(-1, -1)$. Hence, the quadruply degenerate states at the S point with eigenvalues $(+i, -i, +i, -i)$ will separate into two pairs of doubly degenerate states along the SR path with eigenvalues $(+i, +i)$ and $(-i, -i)$, respectively, as shown in Fig. 3(a). As a consequence, along the UR path, two pairs of bands have

to switch partners and cross each other, forming the typical hourglasslike structure. Along arbitrary loops connecting the U and R points in this plane, the crossing point always exists, and its trace naturally forms one quarter of the nodal line in the plane, as shown in Fig. 3(b). A significant difference between this type of nodal line [Fig. 1(b)] and other nodal lines [Fig. 1(a)] is that a double Dirac point S exists. The nodal line starts at the S point, crosses the UR line, and comes back to another S point, which forms a nodal chain in the extended BZ. It is worth noting that the double Dirac point plays a crucial role in forming the nodal chain structure.

Similarly, for the $g_1 = \{M_z|\boldsymbol{a}/2\}$ operation on its invariant plane $X\Gamma YS$ ($k_z = 0$), using the commutation relation of g_4 and g_1, we find that two degenerate bands possess the same eigenvalues at the Y point and opposite eigenvalues at the X point, as shown in Fig. 3(c). Thus, an HNC is also expected in this plane. Finally, the HNCs in two mutually perpendicular planes link together at the S point, forming the HNN structure, as demonstrated in Fig. 2(f). In addition, on the $RTYS$ ($k_y = \pi$) plane, both conduction bands and valence bands are doubly degenerate due to the $g_4 = \{C_{2y}|\boldsymbol{a}/2 + \boldsymbol{b}/2 + \boldsymbol{c}/2\}$ operation. They touch each other at the S point, forming a double Dirac cone with linear dispersion, as shown in Fig. 3(d).

V. THE SURFACE STATES OF Ag_2BiO_3

Based on the maximally localized Wannier function (MLWF) methods [38,39], we calculate the surface energy spectrum on different surfaces, as shown in Figs. 3(e) and 3(f). For the (001) surface, the HNC on the $k_z = 0$ plane projects into this surface. As in Fig. 3(e), we can see that inside the projected region there are drumhead-like surface states with nearly flat dispersion, while there are no surface states outside the projected region, which indicates the topological property of the HNC in the bulk state. The other HNC in the $k_x = \pi$ plane projects into the $\bar{S}\bar{X}$ line and gives only bulk states. For the (100) surface, the HNC in the $k_x = \pi$ plane will project into this surface, and a similar flat surface state emerges, as shown in Fig. 3(f). The HNC at $k_z = 0$ projects into the $\bar{S}\bar{X}$ line and only gives bulk states. The region of the projected HNC is rather sizable in momentum space, and the surface state is close to the Fermi level, which facilitates the observations in experiment.

VI. TIGHT-BINDING MODEL OF Ag_2BiO_3

Considering that the electronic states near the Fermi level mainly originate from the $6s$ orbital of four bismuth atoms, we can use a four-band ting-binding (TB) model to describe the band structure of Ag_2BiO_3. The base set is chosen to be $\{\phi_{i,s}\}$, where $i = 1, 2, 3, 4$ stands for different sites, as shown in Fig. 4(a). The TB model is written as

$$H = \sum_i \varepsilon_i c_i^\dagger c_i + \sum_{i \neq j} t_{ij} c_i^\dagger c_j, \tag{3}$$

where $c_i^\dagger$ (c_j) is the creation (annihilation) operator of electrons at site i (j), t_{ij} is the hopping parameter between the ith and jth atoms, and ε_i is the on-site energy of ith site.

As shown in Fig. 4(a), we consider two nearest-neighbor (NN) hoppings (t_1, t_2) and one next-nearest-neighbor (NNN)
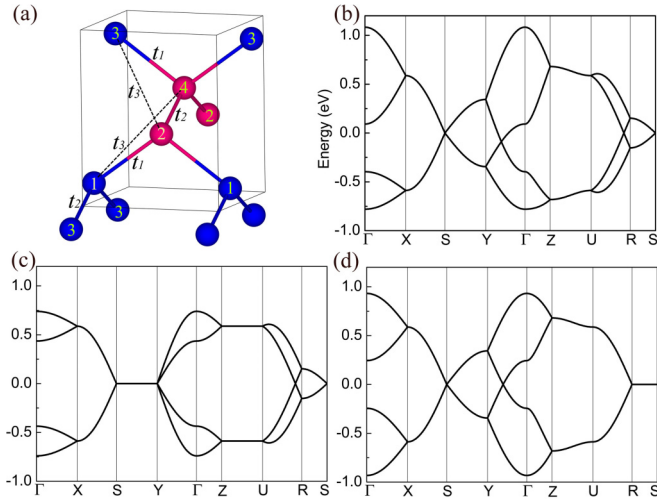
FIG. 4. (a) The lattice with four bismuth atoms for the TB model. t_1 is the NN hopping between sites 1 and 2 and 3 and 4. t_2 is the NN hopping between sites 2 and 4 and 1 and 3. t_3 is the NNN hopping between sites 1 and 4 and 2 and 3. (b) TB band structure ($t_1 = -0.294$ eV, $t_2 = -0.172$ eV, $t_3 = 0.038$ eV, $\varepsilon_i = 0.0$ eV). (c) TB band structure with the same parameters as (b) except $t_2 = 0.0$ eV. (d) TB band structure with the same parameters as (b) except $t_3 = 0.0$ eV.

hopping (t_3). By fitting those hopping parameters, we find the band structure from the TB model matches the density functional theory (DFT) result well. Especially, it can well reproduce the HNN structure in Fig. 4(b). In addition, we reveal that the NN hopping t_2 is responsible for the formation of the HNC on the $X\Gamma YS$ plane. In Fig. 4(c), when t_2 gradually decreases to zero, the HNC on the $X\Gamma YS$ plane will be compressed and finally transform into a fourfold-degenerate nodal line along the SY path, while the HNC on the $XURS$ plane is maintained. The HNC on the $XURS$ plane is dominated by NNN hopping; it will transform into a fourfold-degenerate nodal line along the RS path when $t_3 = 0$, as shown in Fig. 4(d). This transformation from HNC to nodal line is accompanied by a change in symmetry.

VII. SOC EFFECT ON THE HNN

In the presence of SOC, bands are conventionally Kramers degenerate due to the coexistence of time-reversal and space-inversion symmetries. A pair of Kramers degenerate states at each k point can generally be written as $|\phi\rangle$ and $PT|\phi\rangle$. To determine whether the HNN structure can still exist, we need to recalculate the eigenvalues of corresponding symmetries for all bands under the SOC condition.

At the $k_x = \pi$ plane, we can use the eigenvalues $g_\pm = \pm i e^{i(k_y/2+k_z/2)}$ of $g_3 = \{M_x | \boldsymbol{b}/2 + \boldsymbol{c}/2\}$ to identify each band. Suppose a state $|\phi\rangle$ has an eigenvalue g_+, which satisfies $g_3|\phi\rangle = +i e^{i(k_y/2+k_z/2)}|\phi\rangle$. Using the commutation relation $g_3 P = e^{ik_y+ik_z} P g_3$, we find the Kramers partner $PT|\phi\rangle$ satisfies $g_3 PT|\phi\rangle = e^{ik_y+ik_z} PT g_3|\phi\rangle = -i e^{i(k_y/2+k_z/2)} PT|\phi\rangle$, which indicates $PT|\phi\rangle$ has the eigenvalue g_-. Therefore, we find that a pair of Kramers degenerate bands must have opposite eigenvalues of g_3,
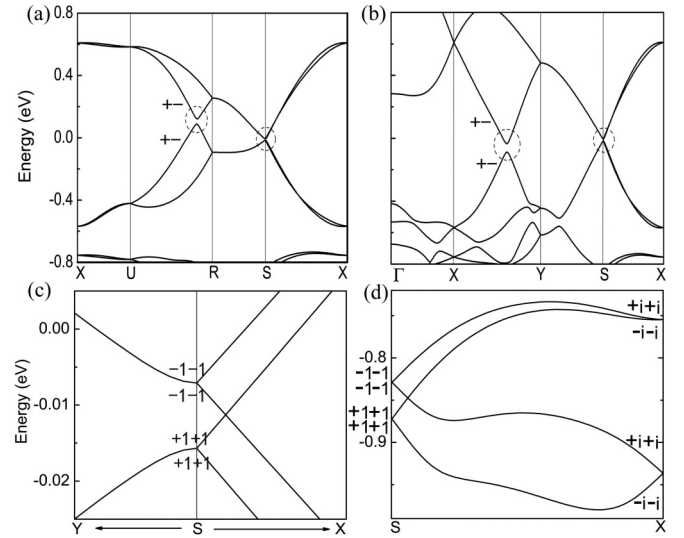
FIG. 5. (a) and (b) Band structures from DFT including SOC. There are gaps inside the dashed circles. (c) The enlarged band structure around the S point near the Fermi level. (d) The hourglasslike band structure along SX below the Fermi level. The eigenvalues of $\{C_{2y} | \boldsymbol{a}/2 + \boldsymbol{b}/2 + \boldsymbol{c}/2\}$ are given.

as shown in Fig. 5(a). Consequently, if two pairs of bands touch each other, g_3 cannot protect a fourfold degeneracy, and gaps are generally opened between bands with the same eigenvalues. Through similar symmetry analysis, we find $g_1 = \{M_z | \boldsymbol{a}/2\}$ cannot protect a fourfold degeneracy on the $k_z = 0$ plane. Thus, we conclude that the HNCs (without SOC) on two planes will be gapped out by the SOC effect. As shown in Figs. 5(a) and 5(b), because of the relatively weak SOC effect of s orbitals, the band gaps induced by SOC are about 51 meV along UR, 33 meV along XY, and 8 meV at the S point, respectively.

On the other hand, along the SX path, we discover that a pair of conduction bands switches one partner with a pair of valence bands and inevitably forms an hourglasslike Dirac semimetal (HDSM) [49] structure, as shown in Fig. 5(c). This process happens for every group of four Kramers pairs in the whole energy range displayed in Fig. 5(d). To reveal the formation of a HDSM, we focus on the $g_4 = \{C_{2y} | \boldsymbol{a}/2 + \boldsymbol{b}/2 + \boldsymbol{c}/2\}$ operation acting on Bloch states on the SX path. We can use its eigenvalues $g_\pm = \pm i e^{ik_y/2}$ to label all bands. Utilizing the condition $g_4 P = -e^{ik_y} P g_4$, we can verify that two Kramers degenerate bands must have the same eigenvalues of g_4 along SX. Therefore, in Fig. 5(d), a pair of Kramers bands with eigenvalues $(+i, +i)$ at the X point must be degenerate with a pair of bands with eigenvalues $(-i, -i)$ since T can interchange i and $-i$ states. Then, for the Bloch states at the S point, a fourfold degeneracy can be derived by the anticommutation relation $\{g_1, P\} = 0$, analogous to the proof of the fourfold degeneracy at the S point in the above spinless case. Moreover, because g_4 commutes with both g_1 and P at the S point, we can conclude that a fourfold-degenerate Bloch state must have the same eigenvalues of g_4, as shown in Fig. 5(d). Finally, along the SX path, four pairs of Kramers degenerate bands have to switch partners and inevitably cross each other, forming an hourglasslike dispersion relation. There

is a symmetry-enforced Dirac point that cannot be eliminated as long as the symmetry remains, which is distinct from the Dirac semimetals protected by pure rotation symmetries that only appear during topological phase transitions [50]. If the electron filling number is $8n + 4$ [13], the Dirac point of a HDSM can perfectly cross the Fermi level in principle.

VIII. CONCLUSIONS AND DISCUSSION

In summary, we reported an HNN structure in Ag_2BiO_3 with a centrosymmetric nonsymmorphic space group in the absence of SOC. The HNN structure is constructed by two HNCs, which are symmetry enforced and cannot be removed without breaking symmetries. From this perspective, this kind of nodal net is different from the accidental nodal net in AlB_2-type TiB_2 [48], which is protected by spatial inversion, mirror symmetry, and band inversion and can be annihilated by just lifting band positions. The special toruslike Fermi surface on both the electron and hole sides was specifically shown. A four-band tight-binding model was developed to describe the HNN structure, and corresponding drumheadlike surface states were demonstrated on the (100) and (001) surfaces. In addition, when including the SOC effect, the HNNs are slightly gapped, and a pair of Dirac points with hourglasslike dispersions inevitably emerges on a twofold screw axis.

It is known that an electron can pick up a nontrivial π Berry phase around a loop that interlocks with the nodal line which may be probed by the Shubnikov–de Haas quantum oscillations in experiment [51]. It has been revealed [52] that the total phase shift for each frequency component of the quantum oscillation depends on the extreme cross sections of the Fermi surface, the direction of the magnetic field, and the sign of the charge carrier. In this respect, it is worth looking forward to observing the abundant phase shift patterns in Ag_2BiO_3 in quantum oscillation experiments due to the unique Fermi surface made of a toruslike electron pocket and a toruslike hole pocket. In addition, we suggest this HNN structure can exist in weak-SOC compounds and bosonic systems with similar nonsymmorphic symmetries.

[1] N. P. Armitage, E. J. Mele, and A. Vishwanath, Rev. Mod. Phys. **90**, 015001 (2018).

[2] H. Weng, X. Dai, and Z. Fang, J. Phys.: Condens. Matter. **28**, 303001 (2016).

[3] M. Z. Hasan, S.-Y. Xu, and B. Guang, Phys. Scr. **T164**, 014001 (2015).

[4] B. Yan and C. Felser, Annu. Rev. Condens. Matter Phys. **8**, 337 (2017).

[5] M. Hirayama, R. Okugawa, and S. Murakami, J. Phys. Soc. Jpn. **87**, 041002 (2018).

[6] A. A. Burkov, M. D. Hook, and L. Balents, Phys. Rev. B **84**, 235126 (2011).

[7] C.-K. Chiu and A. P. Schnyder, Phys. Rev. B **90**, 205136 (2014).

[8] C. Fang, Y. Chen, H.-Y. Kee, and L. Fu, Phys. Rev. B **92**, 081201 (2015).

[9] C. Fang, H. Weng, X. Dai, and Z. Fang, Chin. Phys. B **25**, 117106 (2016).

[10] M. Phillips and V. Aji, Phys. Rev. B **90**, 115111 (2014).

[11] R. Yu, Z. Fang, X. Dai, and H. Weng, Front. Phys. **12**, 127202 (2017).

[12] S.-Y. Yang, H. Yang, E. Derunova, S. S. P. Parkin, B. Yan, and M. N. Ali, Adv. Phys.: X **3**, 1414631 (2018).

[13] R. Takahashi, M. Hirayama, and S. Murakami, Phys. Rev. B **96**, 155206 (2017).

[14] J. Hu, Z. Tang, J. Liu, X. Liu, Y. Zhu, D. Graf, K. Myhro, S. Tran, C. N. Lau, J. Wei *et al.*, Phys. Rev. Lett. **117**, 016602 (2016).

[15] M. Neupane, I. Belopolski, M. M. Hosen, D. S. Sanchez, R. Sankar, M. Szlawska, S.-Y. Xu, K. Dimitri, N. Dhakal, P. Maldonado *et al.*, Phys. Rev. B **93**, 201104 (2016).

[16] G. Bian, T.-R. Chang, R. Sankar, S.-Y. Xu, H. Zheng, T. Neupert, C.-K. Chiu, S.-M. Huang, G. Chang, I. Belopolski *et al.*, Nat. Commun. **7**, 10556 (2016).

[17] B. Feng, B. Fu, S. Kasamatsu, S. Ito, P. Cheng, C.-C. Liu, Y. Feng, S. Wu, S. K. Mahatha, P. Sheverdyaeva *et al.*, Nat. Commun. **8**, 1007 (2017).

[18] Y. Kim, B. J. Wieder, C. L. Kane, and A. M. Rappe, Phys. Rev. Lett. **115**, 036806 (2015).

[19] R. Li, H. Ma, X. Cheng, S. Wang, D. Li, Z. Zhang, Y. Li, and X.-Q. Chen, Phys. Rev. Lett. **117**, 096401 (2016).

[20] N. B. Kopnin, T. T. Heikkilä, and G. E. Volovik, Phys. Rev. B **83**, 220503 (2011).

[21] H. Yang, R. Moessner, and L.-K. Lim, Phys. Rev. B **97**, 165118 (2018).

[22] W. B. Rui, Y. X. Zhao, and A. P. Schnyder, Phys. Rev. B **97**, 161113 (2018).

[23] R. Yu, H. Weng, Z. Fang, X. Dai, and X. Hu, Phys. Rev. Lett. **115**, 036807 (2015).

[24] J. Zhao, R. Yu, H. Weng, and Z. Fang, Phys. Rev. B **94**, 195104 (2016).

[25] Y. Du, F. Tang, D. Wang, L. Sheng, E.-j. Kan, C.-G. Duan, S. Y. Savrasov, and X. Wan, npj Quantum Mater. **2**, 3 (2017).

[26] Q. Xu, R. Yu, Z. Fang, X. Dai, and H. Weng, Phys. Rev. B **95**, 045136 (2017).

[27] A. Yamakage, Y. Yamakawa, Y. Tanaka, and Y. Okamoto, J. Phys. Soc. Jpn. **85**, 013708 (2015).

[28] L. S. Xie, L. M. Schoop, E. M. Seibel, Q. D. Gibson, W. Xie, and R. J. Cava, APL Mater. **3**, 083602 (2015).

[29] S. M. Young and C. L. Kane, Phys. Rev. Lett. **115**, 126803 (2015).

[30] T. Bzdušek, Q. Wu, A. Rüegg, M. Sigrist, and A. A. Soluyanov, Nature (London) **538**, 75 (2016).

[31] S.-S. Wang, Y. Liu, Z.-M. Yu, X.-L. Sheng, and S. A. Yang, Nat. Commnu. **8**, 1844 (2017).

[32] B.-J. Yang and N. Nagaosa, Nat. Commun. **5**, 4898 (2014).

[33] G. Kresse and J. Hafner, Phys. Rev. B **49**, 14251 (1994).

[34] G. Kresse and J. Furthmüller, Phys. Rev. B **54**, 11169 (1996).

[35] P. E. Blöchl, Phys. Rev. B **50**, 17953 (1994).

[36] J. P. Perdew, K. Burke, and M. Ernzerhof, Phys. Rev. Lett. **77**, 3865 (1996).

[37] N. Marzari and D. Vanderbilt, Phys. Rev. B **56**, 12847 (1997).

[38] I. Souza, N. Marzari, and D. Vanderbilt, Phys. Rev. B **65**, 035109 (2001).

[39] Q. Wu, S. Zhang, H.-F. Song, M. Troyer, and A. A. Soluyanov, Comput. Phys. Commun. **224**, 405 (2017).

[40] S. Deibele and M. Jansen, J. Solid State Chem. **147**, 117 (1999).

[41] C. P. Oberndorfer, R. E. Dinnebier, R. M. Ibberson, and M. Jansen, Solid State Sci. **8**, 267 (2006).

[42] X.-J. Liu, S. Zhang, P. Chai, and J. Meng, Chem. Phys. Lett. **446**, 281 (2007).

[43] J. He, D. D. Sante, R. Li, X.-Q. Chen, J. M. Rondinelli, and C. Ranchini, Nat. Commun. **9**, 492 (2018).

[44] B. J. Wieder, Y. Kim, A. M. Rappe, and C. L. Kane, Phys. Rev. Lett. **116**, 186402 (2016).

[45] A. Bouhon and A. M. Black-Schaffer, Phys. Rev. B **95**, 241101 (2017).

[46] Y. Sun, Y. Zhang, C.-X. Liu, C. Felser, and B. Yan, Phys. Rev. B **95**, 235104 (2017).

[47] R. Yu, Q. Wu, Z. Fang, and H. Weng, Phys. Rev. Lett. **119**, 036401 (2017).

[48] X. Feng, C. Yue, Z. Song, Q. Wu, and B. Wen, Phys. Rev. Mater. **2**, 014202 (2018).

[49] B. J. Wieder and C. L. Kane, Phys. Rev. B **94**, 155108 (2016).

[50] S. Murakami, New J. Phys. **9**, 356 (2007).

[51] G. P. Mikitik and Y. V. Sharlai, Phys. Rev. Lett. **82**, 2147 (1999).

[52] C. Li, C. M. Wang, B. Wan, X. Wan, H.-Z. Lu, and X. C. Xie, Phys. Rev. Lett. **120**, 146602 (2018).